ACS APPLIED MATERIALS & INTERFACES

Research Article

www.acsami.org

SiO_2–RuO_2: A Stable Electrocatalyst Support

Chih-Ping Lo and Vijay Ramani*

Center for Electrochemical Science and Engineering Department of Chemical and Biological Engineering, Illinois Institute of Technology, 10 W 33rd Street, Chicago, Illinois 60616, United States

Supporting Information

ABSTRACT: High surface area SiO_2–RuO_2 (SRO) supports with various SiO_2: RuO_2 ratios were synthesized using a wet chemical method. The supports were catalyzed by depositing platinum nanoparticles on their surface. The synthesized materials were characterized by XRD, TEM, BET, and linear sweep voltammetry to study microstructure and properties. The electrochemical stability, electrochemical surface area, electrocatalytic activity and fuel cell performance were also measured. The optimal 1:1 mol ratio of SiO_2–RuO_2 (SRO-1) possessed a BET surface area of 305 m^2/g and an electrical conductivity of 24 S/cm. This SRO support demonstrated 10-fold higher electrochemical stability than Vulcan XC-72R carbon when subjected to an aggressive accelerated stability test (AST) involving 10,000 potential cycles between 1 and 1.5 V. The mass activity of Pt-doped SRO-1 was 54 mA/mg_{Pt}, whereas its specific activity was 115 $\mu A\ cm_{Pt}^{-2}$. The fuel cell performance obtained with this catalyst was lower, but compared favorably against a commercial Pt/C baseline. Analysis of fuel cell performance data confirmed that the lower fuel cell performance resulted largely from ohmic and mass transport losses within the unoptimized electrocatalyst layer.

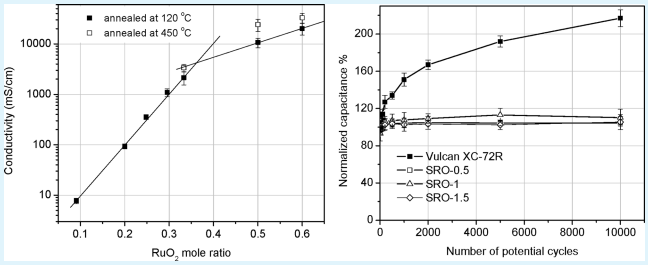

KEYWORDS: *electrocatalyst support, noncarbon support, polymer electrolyte fuel cell, carbon corrosion, metal oxide*

INTRODUCTION

Polymer electrolyte fuel cells (PEFCs) have the potential to alleviate major problems associated with the production and consumption of energy. In contrast to a focus on performance during the early development of PEFCs, current research has been expanded to investigate the improvement of fuel cell reliability and durability.[1−4] One of the major factors affecting the lifetime of PEFCs is carbon corrosion.[5] Carbon is commonly used as a catalyst support for PEFCs because of its large surface area, high electrical conductivity, and favorable pore structure, stabilizing high nanoparticle dispersion. However, carbon will oxidize to CO_2, as indicated by the following reaction[6]

$$C + 2H_2O \rightarrow CO_2 + 4H^+ + 4e^-$$

$$E^o = 0.207\ V\ vs\ NHE,\ 25°C$$

Oxidation of the carbon support is thermodynamically favored during fuel cell operation; the rate of this reaction can increase significantly under certain transient conditions (e.g., start-up/shut-down; fuel starvation).[7] The local electrode potential at the anode and/or the cathode can escalate up to 1.5 V under these transient conditions, resulting in an extremely large overpotential (and hence high reaction rate) for the carbon oxidation reaction.[8] The resultant irreversible loss of carbon causes the release of Pt nanoparticles, which become electrically isolated, leading to a lower Pt utilization as well as diminished fuel cell performance.[9,10] Carbon corrosion also causes the agglomeration and sintering of Pt particles, which leads to a loss in the electrochemical surface area (ECSA) of the electrode.[11]

Considerable effort has been expended to develop carbon materials with higher graphitic character to increase stability. These carbon materials include carbon nanotubes,[12,13] nanocoils,[14,15] nanohorns,[16] nanofibers,[17,18] and grapheme.[19] However, these materials still do not prevent irreversible carbon oxidation at high electrode potentials.[20] Therefore, various alternatives, such as metal oxides, carbides and nitrides, have been studied as candidates for oxidation resistant catalyst supports; examples include SnO_2,[21,22] ITO,[23] WO_x,[24,25] TiO_2,[26,27] RuO_2,[28,29] SiO_2,[30,31] WC,[32,33] and WN.[34] Any successful alternative support material should demonstrate the following properties: (i) high surface area; (ii) suitable porosity; (iii) high electrical conductivity, and (iv) high stability at low pH under fuel cell operation conditions.[35]

SiO_2 has been used in fuel cell applications as a filler in composite membranes, which have been prepared following several procedures and employed for PEFCs[36,37] and direct methanol fuel cells (DMFCs).[38] SiO_2/C composite aerogels have been used as catalyst supports to improve the activity.[39] Seger et al. have used silica-supported Pt electrocatalysts for PEM fuel cells.[31] Here, the SiO_2 was coated with Pt and the Pt–SiO_2 particles were linked together, forming a conducting network. The 2:1 ratio of Pt: SiO_2 particles attained both high

Received: August 21, 2012
Accepted: October 11, 2012
Published: October 11, 2012

conductivity and high surface area. With an increase in the ratio of Pt to SiO_2, the platinum particles tended to aggregate. The stability of this support was not reported.

The objectives of this work were to synthesize and evaluate SiO_2–RuO_2 (SRO) with high electrical conductivity and BET surface area, to determine the applicability of this class of materials as an alternate, corrosion-resistant electrocatalyst support. Ordered mesoporous SiO_2 (SBA-15) was used as a high-surface-area matrix. The electrically conductive RuO_2 component was loaded onto the surface of the high-surface-area silica matrix. SRO with different Si/Ru ratios were synthesized and characterized by XRD, TEM, BET and linear sweep voltammetry. The stability of SRO supports and Pt/SRO catalysts were examined using industry-standard accelerated stress test (AST) protocols. Membrane electrode assembles (MEAs) were prepared and evaluated with Pt/SRO catalysts at both the cathode and the anode, because carbon corrosion can occur at both anode and cathode.[7] The sources of polarization in MEAs prepared using Pt/SRO electrocatalysts were analyzed and are presented.

EXPERIMENTAL SECTION

Materials. The following chemicals were used as received: Pluronic P-123, hydrochloric Acid, (HCl, 37% Fisher), tetraethyl orthosilicate (TEOS, 99%, Sigma-Aldrich), ruthenium(III) chloride hydrate ($RuCl_3.xH_2O$, 35–40% Ru, Acros Organics), chloroplatinic acid hexahydrate ($H_2PtCl_6{\cdot}6H_2O$, ACS reagent, ≥37.50% Pt basis, Sigma-Aldrich), formic acid (HCOOH, ∼98%, Fluka), potassium hydroxide (KOH, ACS, Fisher), 5 wt % Nafion (1100 EW, Solution Technologies, Mendenhall, PA).

Preparation of SiO_2–RuO_2 (SRO). High-surface-area SiO_2 (SBA-15) was synthesized as follows - Pluronic 123 (3.1 mmol) was dissolved under stirring in DI water (560 g) and concentrated HCl (100 g) at room temperature. TEOS (0.19 mol) was added to the solution and stirred for 5 min, followed by stirring at 35 °C for 20 h. The mixture was aged at 80 °C for 24 h. The precipitate was filtered and dried at 60 °C for 24 h. The resultant powder was annealed to remove Pluronic 123 using the following temperature profile: (1) heating to 200 °C at 1 °C /min, (2) holding at 200 °C for 1 h, (3) heating to 550 oC at 1 °C /min, (4) holding at 550 °C for 6 h, and (5) cooling to 200 °C at 1 °C /min. This yielded SBA-15 silica. SiO_2–RuO_2 (SRO) was prepared by depositing RuO_2 on the resultant silica support. The SBA-15 was immersed in an aqueous solution containing 0.1 M $RuCl_3{\cdot}nH_2O$. 0.1 M KOH (aq) was dropped into the mixture under stirring until the pH of the solution reached seven. The resultant black powder was filtered out and washed repeatedly with distilled water. The solid was dried at 120 °C and annealed at 450 °C. Different composites with RuO_2 to SiO_2 mole ratios of 1.5, 1, 0.5, 0.42, 0.33, 0.25, 0.1, and 0 were synthesized using this method. In the accompanying discussion, the synthesized supports are denoted as SRO-a, where a represents the mole ratio.

Preparation of Pt/RuO_2–SiO_2 Catalysts. Platinum nanoparticles were synthesized by the chemical reduction of chloroplatinic acid with formic acid.[40] In a typical synthesis, a suspension of 5 mmol of SRO in reaction solution (1.9 mmol of $H_2PtCl_6{\cdot}6H_2O$ and 30 mL of HCOOH in 600 mL of water) was sonicated for 30 min. All aqueous solutions were prepared with DI water from a Millipore water system. After this initial dispersion, the solution was heated at 80 °C for 2 h under vigorous stirring. The product was collected by vacuum filtration and washed several times with DI water, and then dried in an oven at 120 °C. The catalyst was denoted as 40% Pt/SRO.

Characterization Techniques. X-ray diffraction (XRD) was performed using a Rigaku Miniflex diffractometer to confirm the presence of ruthenium oxide and platinum and to estimate platinum crystallite size. Diffractograms were recorded in the range $2\theta = 20–80°$ with a step of 2°/min.

Transmission electron microscopy (TEM) was used to determine the size and distribution of the platinum particles and support aggregates. TEM micrographs were obtained using a Jeol 2100F microscope equipped with a liquid nitrogen Si (Li) EDX detector, at an acceleration voltage of 200 kV.

A Brunauer–Emmett–Teller (BET) surface area analyzer was used to calculate the BET specific surface area by a multipoint analysis of nitrogen desorption isotherms.

The two-point probe technique was used in conjunction with linear-sweep voltammetry to measure the electrical conductivity of the supports. All experiments were conducted at room temperature.

Evaluation of Electrochemical Surface Area (ECSA). Electrochemical characterization was performed in a three-compartment electrochemical cell in 0.1 M $HClO_4$: The support/catalyst material of interest was made into an ink and deposited onto a glassy carbon disk (0.196 cm^2) to yield a thin film. This was used as the working electrode; a saturated calomel electrode (SCE) was used as the reference electrode; a Pt foil was used as the counter electrode. Details about ink preparation and deposition are provided in the Supporting Information.

The electrolyte was purged with nitrogen gas for 30 min before the measurement. Due to minor contamination from the binder, the electrode potential was cycled 20 times at a scan rate of 100 mV/s between 0.05 and 1.2 V vs NHE to produce a clean surface. Subsequently, a cyclic voltammogram (CV) was measured by scanning the working electrode potential between 0.05 and 1.2 V vs NHE at a scan rate of 20 mV/s.

The ECSA were calculated by measuring the charge associated with hydrogen desorption (C) between 0.05 and 0.4 V vs NHE and assuming 210 $\mu C\ cm^{-2}$ as the conversion factor corresponding to the charge associated with the adsorption of one monolayer of hydrogen on the surface of polycrystalline platinum.[41] The ECSA of Pt was calculated on the basis of the relation

$$\mathrm{ECSA} = \left[\frac{C}{210 L_{\mathrm{Pt}} A_{\mathrm{g}}}\right] \times 10^5$$

Where L_{Pt} is the loading of Pt ($mg_{Pt}\ cm^{-2}$) on the working electrode and A_g (cm^2) is the geometric area of the working electrode.

Evaluation of Stability Using Accelerated Stability Test (AST) Protocols. The AST protocols (start–stop and load cycling protocols)[42] employed in this study are as follows: For evaluating the stability of the support (support corrosion), the working electrode potential was cycled between 1 to 1.5 V vs NHE at a scan rate of 500 mV/s for 10,000 cycles. This protocol aggressively simulated the startup-shutdown transients in an operating PEFC (see Figure S1 under the Supporting Information). For evaluating the stability of the electrocatalyst (Pt dissolution), the working electrode potential was cycled between 0.6 and 0.95 V vs NHE for 10 000 cycles to simulate full load-no load transients in an automotive drive cycle (See Figure S2 under the Supporting Information). Both series of tests were performed in nitrogen-saturated electrolyte at room temperature. The support stability test was also performed on the catalyzed support to investigate the impact of platinum catalyst on the corrosion rate. For each AST, CVs were periodically recorded at regular intervals during the test to monitor the extent of support and/or catalyst degradation. Vulcan XC-72 carbon was used as a baseline catalyst support and 46.5% Pt/C obtained from TKK was used as the baseline electrocatalyst for benchmarking purposes.

Preparation of MEAs. MEAs were prepared by spraying multiple layers of catalyst ink directly onto both sides of a Nafion 211 membrane. After both the anode and cathode catalyst layers were applied, the MEAs were hot pressed at 60 °C for 30 s at 2000 psi. All prepared MEAs had an active area of 5 cm^2. The Pt loading at the cathode, estimated gravimetrically, was 0.4 mg/cm^2 and the Pt loading at the anode was 0.2 mg/cm^2. Additional details about ink preparation and MEA preparation are provided under the Supporting Information.

PEFC performance. Polarization curves were obtained using a Compact Fuel Cell Test System model 850C (Scribner Associates, Inc.). The performance testing was conducted at 80 °C with an inlet

relative humidity of 75% (corresponding to a saturator dew point of 73 °C). Stoichiometric ratios of 2 for the anode and cathode, with minimum flows of 0.2 SLPM were employed during testing. Further details about operating conditions and oxidants used are provided under Supporting Information.

RESULTS AND DISCUSSION

X-ray Diffraction (XRD) Measurements. XRD was used to confirm the crystal structure and to obtain a quantitative estimate of the crystallite size. Figure 1 shows the XRD patterns

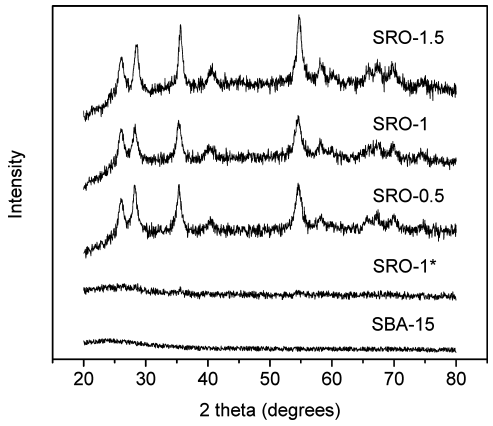

Figure 1. XRD patterns of SRO supports and SBA-15. Supports were annealed at 450 °C. SRO-1* represents the sample annealed at 120 °C.

of SRO supports with different Ru/Si ratios. The as-synthesized SBA15 was in an amorphous phase. No RuO_2 peak was obtained for the materials annealed at 120 °C. For materials annealed at 450 °C, the main diffraction peaks around 28, 36, and 55° arose from diffractions of Rutile RuO_2 (110), (101), and (211) planes, respectively.[43]

The crystallite size was then estimated using the Scherrer equation[44] and the RuO_2 (211) peak. The average RuO_2 crystallite sizes for SRO-0.5, SRO-1, and SRO-1.5 were 8.9, 9.4, and 9.9 nm, respectively. RuO_2 aggregation at higher loadings leading to larger crystallite size was thereby confirmed.

Figure 2 shows the XRD patterns of Pt deposited on the SRO supports. All catalyst samples had crystalline Pt particles. The main diffraction peaks around 39, 46, and 68° arose from diffractions at Pt (111), (200) and (220) planes, respectively.[45]

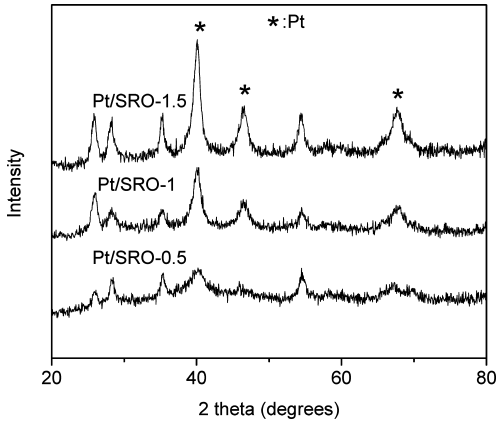

Figure 2. XRD patterns of Pt/SRO. The SRO supports were annealed at 450 °C.

The crystallite size was then estimated using the Scherrer equation[44] and the Pt (111) peak. The average Pt crystallite sizes for Pt/SRO-0.5, Pt/SRO-1, and Pt/SRO-1.5 were 4.5, 7.7, and 9.4 nm, respectively. This observation confirmed that supports with higher BET surface area yielded Pt particles with smaller crystallite sizes (see also discussion below under BET Surface Area).

TEM. The surface morphology and dispersion of Pt particles on the synthesized supports were examined by TEM. Figure 3 shows high-resolution TEM images of Pt/SRO-0.5, Pt/SRO-1 and Pt/SRO-1.5 catalysts. The Pt particle sizes were on the order of 3−5, 4−7, and 8−12 nm, respectively, for Pt/SRO-0.5, Pt/SRO-1, and Pt/SRO-1.5, respectively. The results were in agreement with the Pt crystallite sizes estimated from XRD.

Electrical Conductivity. The electrical conductivity of support materials annealed at 120 and 450 °C was measured at room temperature (Figure 4, Table 1). The materials annealed at 450 °C showed higher electrical conductivity, which was attributed to the improved crystallinity induced during the annealing process (see Figure 1).

As shown in Figure 4, the conductivity of the SRO support increased with RuO_2 loading within the silica matrix. The rate of increase in conductivity with RuO_2 loading at RuO_2 to RuO_2 + SiO_2 mole ratios below 0.35 was greater than the corresponding rate at larger RuO_2 to RuO_2 + SiO_2 mole ratios. This difference rate of increase was attributed to the amount of particle contact required for creating optimal pathways to conduct electrons. Increasing RuO_2 content at lower RuO_2 loadings created substantially more pathways for electron conduction, resulting in near percolation at the break point (a loading corresponding to 0.35 mol ratio). Further addition of RuO_2 above a certain loading did not add significantly more pathways. Similar percolation behavior has been seen in other systems.[46]

BET Surface Area. The BET surface areas obtained for the various samples synthesized are presented in Table 1. The BET surface area of all SRO variants was much less than pure SBA-15 and the surface area of SRO decreased with increasing RuO_2 loading. This observation was attributed to the facts that the RuO_2 was denser than SiO_2 and that the porous surface of SBA-15 was blocked by the deposited RuO_2 molecules.[47] The deposited RuO_2 first filled the micropores of SBA-15 (<2 nm), which resulted in a lower BET surface area compared to pristine SiO_2. With the increase in RuO_2 loading, the deposited RuO_2 blocked the mesopores of SBA-15 (2−50 nm), which caused further decrease in surface area. Nonetheless the surface area of the SRO-1 was as high as 305 m^2/g, which is greater than that of a typical graphitized carbon. The samples retained their surface area upon annealing.

ELECTROCHEMICAL CHARACTERIZATION

Support Stability. The CVs recorded for Vulcan XC-72 carbon during the accelerated support stability test (1−1.5 V vs NHE; 10 000 cycles)[42] showed evidence of substantial surface oxide formation through increased peak current assigned to the hydroquinone−quinone (HQ−Q) redox couple of carbon[48] (Figure S3, Supporting Information). On the other hand, the CVs remained essentially unchanged upon cycling up to 10 000 cycles for the SRO supports (see Figures S4−S6 in the Supporting Information). These results suggested that the RuO_2 with an Ru oxidation state of IV was electrochemically stable under this aggressive AST, which agreed with prior reports.[49] The capacitance of the support (calculated from the

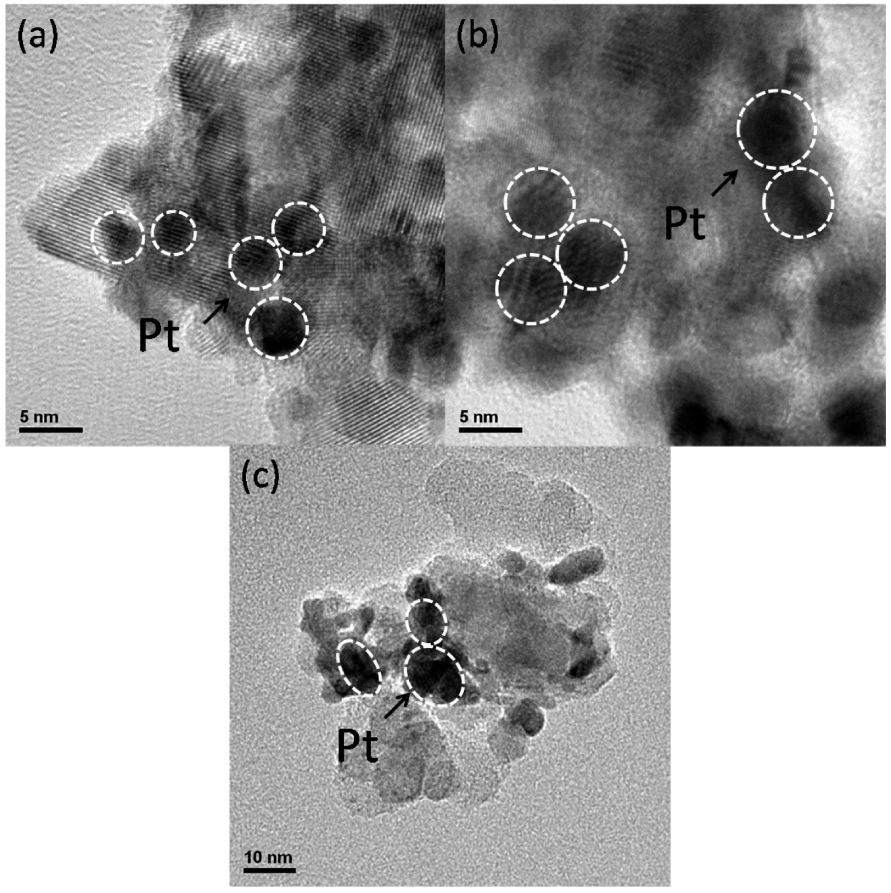

Figure 3. TEM images of (a) Pt/SRO-0.5 (b) Pt/SRO-1, and (c) Pt/SRO-1.5.

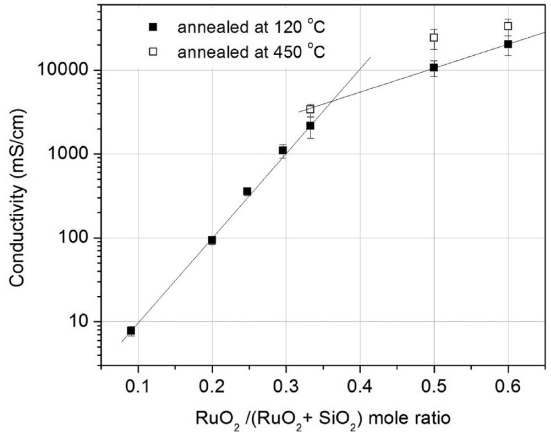

Figure 4. Electrical conductivity of SRO annealed at 120 and 450 °C.

CV) was used as a measure of support surface area and monitored as a function of cycle number (Figure 5). Although carbon showed a change in capacitance of more than 100%, the observed change in the capacitance (normalized to initial value) was only ±10% for the SRO supports. This confirmed the exceptional electrochemical stability of the SRO supports even under extremely stringent test conditions.

Catalyst Stability. Several factors can cause a lowering in ECSA, including support corrosion, Pt dissolution and redeposition via Ostwald ripening, and Pt aggregation.[9,10] The durability of the catalyzed supports was evaluated by monitoring the change in ECSA (normalized to initial ECSA) as a function of cycle number under the load cycling protocol (0.6−0.95 V vs NHE).[42]

Table 1. Electrical Conductivity and BET Surface Area of the SRO Samples

sample	electrical conductivity (S/cm)	BET surface area (m^2/g)
Vulcan XC-72	31 ± 5	207 ± 4
SRO-0	~0	1057 ± 89
SRO-0.1	$7.7 \pm 1 \times 10^{-3}$	470 ± 34
SRO-0.25	$9.4 \pm 1 \times 10^{-2}$	460 ± 62
SRO-0.33	$3.6 \pm 0.4 \times 10^{-1}$	460 ± 39
SRO-0.42	1.1 ± 0.2	440 ± 27
SRO-0.5	2.1 ± 0.6/3.3 ± 0.5[a]	430 ± 21/420 ± 38[a]
SRO-1	12 ± 1/24 ± 6[a]	290 ± 18/305 ± 42[a]
SRO-1.5	20 ± 5/33 ± 8[a]	220 ± 17/195 ± 8[a]

[a]The sample annealed at 450 °C.

All Pt/SRO catalysts demonstrated higher stability than the baseline Pt/C electrocatalyst, as seen from the normalized ECSA values presented in Figure 6. The electrocatalyst stability apparently improved with an increase in the RuO_2 content. Given that the SRO supports were not designed in any way to mitigate any of the platinum degradation mechanisms, the trend seen was attributed to the fact that all the SRO supports yielded electrocatalysts with larger platinum particle sizes than the Pt/C benchmark. Because the larger particles had lower surface free energies, they demonstrated a smaller propensity to degrade/agglomerate.[50] Thus, the apparent increase in stability was more due to the intrinsic size of the platinum particle than to the support. Note that the absolute value of the ECSA of the

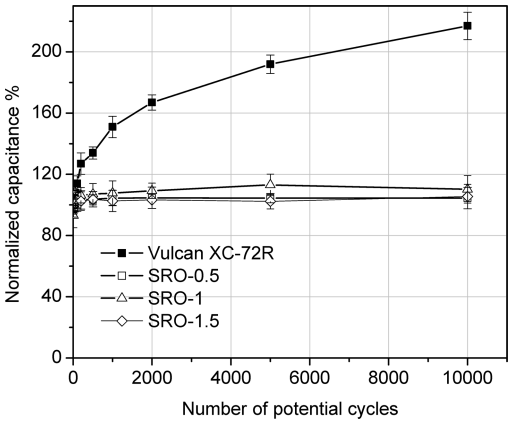

Figure 5. Change of normalized capacitance of the catalyst supports as a function of cycle number.

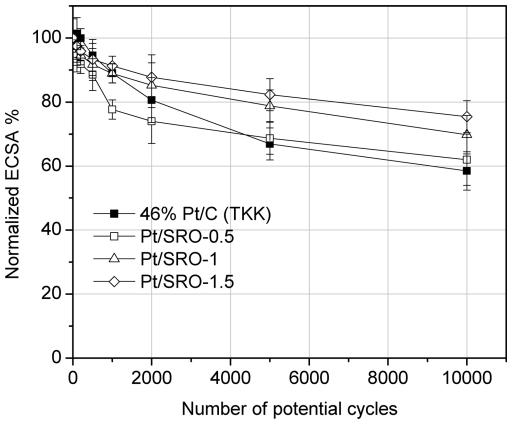

Figure 6. Loss of ECSA of the catalysts as a function of cycle numbers.

Pt/C catalyst was still higher than that of the Pt/SRO catalysts after the AST tests.

The capacitive current at potentials between 0.4 and 0.6 V due to charging/discharging of the double layer was recorded while performing the accelerated load cycling test on the catalyzed supports. The capacitive current remained the same for all tested catalysts over 10 000 cycles (see Figures S7–S10 in the Supporting Information). The results confirmed that the SRO and C supports did not corrode under the AST protocol and confirmed that the ECSA degradation was primarily due to dissolution/aggregation of platinum, and not due to support corrosion.

Platinum has been reported to accelerate the rate of carbon support corrosion.[51] The durability of Pt/SRO-1 was evaluated under the start–stop cycling protocol to examine the impact of addition of platinum on the rate of support corrosion. The CVs obtained (and the effective capacitance) remained identical before and after the AST test (see Figure S11 in the Supporting Information). This result confirmed that SRO was electrochemically stable and that the added platinum did not catalyze the SRO support corrosion, unlike in carbon supports.

Fuel Cell Performance and Polarization Data Analysis. The performance obtained from MEAs prepared with Pt/SRO-0.5, Pt/SRO-1, and Pt/SRO-1.5 as well as 46.5 wt % Pt/C (TKK), with air as the oxidant, are shown in Figure 7. The polarization data obtained on these MEAs with four different oxidants (O_2, air, Helox and 4% O_2) are plotted in Figures S12–S15 in the Supporting Information.

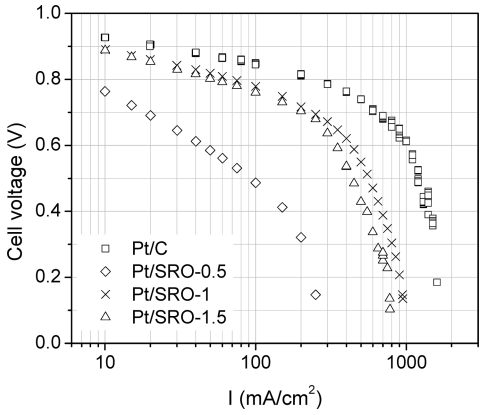

Figure 7. Polarization data for H_2/air PEFCs with different catalysts at 80 °C, 75% RH and ambient pressure. Two times stoichiometric flow rate of reactants. Anode catalyst loading: 0.2 mg/cm^2 and cathode catalyst loading: 0.4 mg/cm^2.

The performance obtained with Pt/SRO-0.5 was significantly lower than Pt/SRO-1 and Pt/SRO-1.5. The polarization data obtained was analyzed following the method initially proposed by Williams et al.[52] and subsequently utilized by Sambandam et al.[53,54] The analysis is briefly described here, please refer to Williams et al.,[52] for details. The objective of this analysis was to quantitatively estimate key ohmic, mass transport, and kinetic parameters as well as the distribution of overpotentials in the MEAs prepared using the various electrocatalysts studied. Implementing the methods described, four main sources of polarization losses were estimated: (1) nonelectrode ohmic overpotential ($\eta_{ohmic,\ nonelectrode}$, ohmic losses due to membrane, gas diffusion layer (GDL) and any contact resistances); (2) electrode ohmic overpotential ($\eta_{ohmic,\ electrode}$, ohmic losses in the electrode); 3) nonelectrode concentration overpotential ($\eta_{conc,\ nonelectrode}$, mass transport losses in the GDL and through binder film in the electrode where oxygen is not consumed); (4) electrode concentration overpotential ($\eta_{conc,\ electrode}$, mass transport losses due to combined reaction and diffusion within the electrode where oxygen is consumed). Polarization curves obtained with four different oxidants (O_2, air, Helox, and 4% O_2) were used for this analysis (see Figures S12–S15 in the Supporting Information).

Ohmic Losses. Table 2 reports the overpotential at two different current densities, 200 and 600 mA/cm^2, with air as oxidant, for each MEA. The nonelectrode ohmic overpotential ($\eta_{ohmic,\ nonelectrode}$) was higher for the MEAs prepared with the SRO-based catalysts. Given that all MEAs had the same membrane, in principle, there should have been no variation in membrane resistance. The observed variation was attributed to contact resistances at the membrane electrode interface due to less than ideal binding between the SRO-based catalyst layer and the Nafion membrane. The effective "electrolyte + contact" resistances are reported in Table 3.

The ohmic resistance in the electrode, R_e, was estimated using the data corrected for $\eta_{ohmic,\ nonelectrode}$. Under certain assumptions,[52] the ratios of current density obtained from polarization data of O_2 to that obtained from polarization data of air should be equal to 4.76 (ratio of oxygen concentration O_2 and in air). The polarization data was iteratively adjusted using various R_e values until this condition was satisfied. The calculated R_e values for MEAs prepared using Pt/C, Pt/SRO-0.5, Pt/SRO-1, and Pt/SRO-1.5 were 33, 240, 90, and 140 mΩ

dx.doi.org/10.1021/am3017416 | ACS Appl. Mater. Interfaces 2012, 4, 6109–6116

Table 2. Polarization Sources in Air Operation at 80 °C and 75% RH at Current Densities of 200 mA/cm^2 and 600 mA/cm^2

	Pt/C		Pt/SRO-0.5		Pt/SRO-1		Pt/SRO-1.5	
overpotential (mV)	i = 200	i = 600	i = 200	i = 600	i = 200	i = 600	i = 200	i = 600
$\eta_{ohmic,\ nonelectrode}$	12 ± 1	35 ± 3	20 ± 2	N/A	17 ± 1	50 ± 6	16 ± 2	48 ± 3
$\eta_{ohmic,\ electrode}$	7 ± 0.5	19 ± 1	180 ± 25	N/A	18 ± 2	54 ± 5	50 ± 6	150 ± 12
$\eta_{conc,\ nonelectrode}$	16 ± 2	57 ± 3	57 ± 4	N/A	0	131 ± 21	0	164 ± 18
$\eta_{conc,\ electrode}$	0	0	93 ± 7	N/A	0	55 ± 5	0	81 ± 6
total	35 ± 3.5	111 ± 7	350 ± 38	0	35 ± 3	290 ± 37	66 ± 8	443 ± 39

Table 3. Characteristic Parameters for MEAs at 80°C, 75% RH and Ambient Pressure[a]

	Pt/C	Pt/SRO-0.5	Pt/SRO-1	Pt/SRO-1.5
b (mV/dec)	62 ± 3	124 ± 11	74 ± 4	71 ± 4
i_o (mA/cm^2)	2.93 ± 0.1 × 10^{-3}	1.08 ± 0.1 × 10^{-3}	5.59 ± 0.8 × 10^{-3}	4.07 ± 0.7 × 10^{-3}
j_m (mA mg_{Pt}^{-1})	131 ± 25	11 ± 0.7	54 ± 5	49 ± 6
j_s (μA cm_{Pt}^{-2})	238 ± 31	51 ± 6	115 ± 10	101 ± 8
ECSA (m^2/g)	55 ± 5	22 ± 2	47 ± 5	49 ± 6
nonelectrode ohmic resistance (mΩ cm^2)	58 ± 5	100 ± 10	85 ± 5	80 ± 10
electrode ohmic resistance m (Ω cm^2)	33 ± 2	240 ± 33	90 ± 10	140 ± 17
limiting current, air, (mA cm^2)	1604 ± 118	270 ± 31	980 ± 120	789 ± 89

[a]2 times stoichiometric flow rate of reactants. Anode catalyst loading: 0.2 mg/cm^2 and cathode catalyst loading: 0.4 mg/cm^2.

cm^2, respectively (Table 3). The value obtained for the Pt/C-based electrode was in line with expectations and was largely attributed to the resistance to proton transport in the electrode layer. In the case of SRO-0.5, the high electrode resistance was primarily due to poor electrical conductivity of the support material. Both SRO-1 and SRO-1.5 yielded lower R_e values than SRO-0.5 due to their higher electron conductivity. The higher R_e for SRO-1.5 compared to SRO-1 (despite its higher conductivity) suggested that in addition to electrical conductivity, the distribution of ionomer within the electrode was important. This is governed by the surface properties and the pore structure of the catalyst support, neither of which were optimized in this study.

Mass Transport Losses. To obtain $\eta_{conc,\ nonelectrode}$, the limiting current density (i_{lim}) was estimated for each MEA. The procedure[52] involves altering the i_{lim} iteratively until the plot of $\log(1/(1 - i/i_{lim}))$ vs overpotential (corrected for all ohmic resistances) yielded a straight line. The final i_{lim} values are reported in Table 3. The $\eta_{conc,\ nonelectrode}$ was calculated at each current density by finding the difference in voltage between the initial and corrected curves. The $\eta_{conc,\ nonelectrode}$ was larger for the SRO supports than for the carbon support. Given that the gas diffusion layers used were the same, this observation was attributed to the fact that the SRO supports were significantly denser than carbon, leading to a much thicker binder film layer in the electrode (the binder loading employed was the same for all MEAs). Transport of oxygen through this binder film was hindered, leading to larger $\eta_{conc,\ nonelectrode}$. Within the SRO supports, the magnitude of this overpotential tracked well with the limiting current densities that were estimated by this analysis.

The overpotential due to combined reaction and transport ($\eta_{conc,\ electrode}$) in the cathode was estimated by extrapolating the Tafel slope from the activation region and subtracting this "kinetic" Tafel slope line from the overpotential corrected for all ohmic and nonelectrode concentration losses. To calculate the kinetic Tafel slope, in mV/dec, we used the activation-controlled region where current density was 10−100 mA/cm^2 to ensure that concentration overpotentials, ohmic overpotentials, as well as mixed-potentials could be neglected. In general, SRO supports exhibited higher mass transport losses than carbon support. This was attributed to water retention within the electrode due to the hydrophilic nature of the support.

To identify whether O_2 transport within the various electrodes studied was hindered by gas phase and/or condensed phase diffusion limitations, the helox-air gain was plotted against the O_2−air gain for each current density (Figure 8).[53] If there were no mass transfer limitations, the gain plot

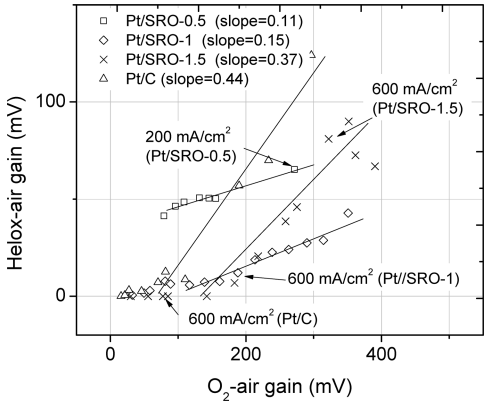

Figure 8. Helox-air gain vs O_2−air gain at 80 °C and 75% RH.

would reduce down to a cluster of points at (48, 0), corresponding to the expected oxygen−air gain of 48 mV.[53] This is unlikely to be realized in practice. Realistically, the current density at which the points begin to deviate from (48, 0) could be considered as a measure of severity of mass-transport losses. The higher this current density, the less severe the mass transport losses. If gas phase diffusion were a limiting factor, a finite helox−air gain would be observed because O_2 diffusivity in helox is higher than that in air.[55] An oxygen−air gain would also be observed, over and above the expected value of 48 mV.[53] Hence, the gain plot would yield a straight line with a positive slope. On the other hand, if condensed phase diffusion were a limiting factor, the helox−air gain would be

dx.doi.org/10.1021/am3017416 | ACS Appl. Mater. Interfaces 2012, 4, 6109−6116

close to zero, whereas the oxygen−air gain would increase, leading to a line with a slope close to zero in the gain plot.[53]

By examining the current densities at which the plots departed from (48, 0) [or alternately, by comparing the position of a fixed current density on the plot], the extent of mass transport losses in the various electrodes was ascertained. The electrode prepared with Pt/C had the lowest mass transport resistance, followed by Pt/SRO-1, Pt/SRO-1.5, and Pt/SRO-0.5. This trend agreed exactly with findings from the polarization data analysis, reported in Table 2. All supports exhibited gas phase mass transport limitations as evidenced by the nonzero slope of the gain plot. Pt/SRO-0.5 and Pt/SRO-1 exhibited a larger propensity toward condensed phase transport limitations (evidenced by their smaller slopes).

Activation Losses. The H_2/O_2 polarization curves corrected for ohmic and nonreacting O_2 transport losses are plotted in Figure 9. The Tafel slope, exchange current density

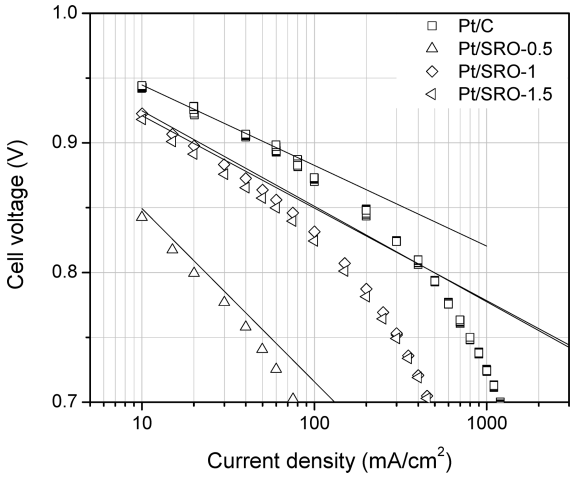

Figure 9. Analysis of H_2/O_2 polarization data for MEAs with Pt/C, Pt/SRO-0.5, Pt/SRO-1, and Pt/SRO-1.5. The straight lines correspond to data corrected for ohmic (membrane+cathode) and nonreacting O_2 transport losses.

(i_o), mass activity ($j_{m,\ 0.9\ V,NHE}$), specific activity ($j_{s,\ 0.9\ V,NHE}$), and ECSA were calculated and are summarized in Table 3. The results obtained for Pt/C (benchmark) agreed with the literature.[56] The Tafel slopes obtained with Pt/C, Pt/SRO-1 and Pt/SRO-1.5 catalysts were close to the theoretical value of 70 mV/dec at 80 °C. The large Tafel slope obtained with Pt/SRO-0.5 indicated either an altered mechanism for the oxygen reduction reaction or the presence of a mixed activation/transport regime, giving rise to a double Tafel slope. The exchange current density of Pt/SRO-0.5 and its ECSA were also lower than the other samples, suggesting intrinsically low activity. The Pt/SRO-1 and Pt/SRO-1.5 catalysts exhibited higher exchange current densities, but lower mass and specific activities than Pt/C, largely because fo their larger platinum particle sizes when compared to Pt/C.

The performance obtained using these catalysts and the initial mass and specific activities obtained in this study are promising when taken in conjunction with the exceptional stability of this support toward oxidative degradation and the fact that minimal optimization of the platinum particle size or electrode structure was performed (contrary to the Pt/C electrode, wherein carbon corrosion was severe and optimized and highly refined electrode formulations were used).

CONCLUSIONS

High-surface-area SiO_2−RuO_2 (SRO) catalyst supports were synthesized using a wet chemical process. The SRO supports exhibited high electrical conductivity (2−20 S/cm) when the RuO_2 − SiO_2 mole ratio was greater than 0.33. The BET surface area of the composite support decreased with increasing loading of RuO_2. The optimal formulation, SRO-1, possessed a BET surface area of 305 m^2/g. SRO supports exhibited much higher (by a factor of at least 10) electrochemical stability than the benchmark carbon material when interrogated using aggressive accelerated test protocols that simulated 10 000 start-up and shut-down cycles. Unlike in carbon, the addition of platinum onto the support did not accelerate the support corrosion rate. The particle size of platinum on the surface of SRO support was on the order of 5−10 nm. The fuel cell performance of MEAs prepared using Pt/SRO was excellent, but was nevertheless lower than that of the Pt/C benchmark. This was attributed to the lower mass activity of the Pt/SRO catalysts (larger Pt particle size) as well as enhanced ohmic and transport losses attributed to the nonoptimized nature of the prepared electrodes (in contrast with the optimized Pt/C benchmark). In closing, the outstanding stability of the support in conjunction with its high surface area, excellent electrical conductivity, and promising activity of derived electrocatalyst renders it an excellent candidate for a corrosion-resistant support, especially for automotive applications.

ASSOCIATED CONTENT

Supporting Information

Details of accelerated stability test (AST) protocols, ink preparation, MEA preparation, and fuel cell operation conditions. Figures: cyclic voltammograms of supports and catalyst, polarization curves obtained using Pt/SRO and Pt/C MEAs. This material is available free of charge via the Internet at http://pubs.acs.org.

AUTHOR INFORMATION

Corresponding Author

*E-mail: ramani@iit.edu. Fax: 312-567-8874. Phone: 312-567-3064.

Funding

This work was supported by the U.S. Department of Energy (DOE), Grant DE-EE0000461.

Notes

The authors declare no competing financial interest.

ACKNOWLEDGMENTS

Guanxiong Wang is acknowledged for contributing to some of the experimental efforts involving support synthesis and characterization. The authors gratefully acknowledge Dr. Kev Adjemian and Dr. Nilesh Dale, Nissan Technical Center, North America, for providing insights into the Accelerated Test Protocols used in this study and for helpful discussions. The authors acknowledge the U.S. Department of Energy for funding.

REFERENCES

(1) Vielstich, W.; Lamm, A.; Gasteiger, H. *Handbook of Fuel Cells − Fundamentals, Technology and Applications*; John Wiley & Sons: Chichester, U.K., 2003; Vol. 3, p 538.

(2) Antolini, E.; Giorgi, L.; Pozio, A.; Passalacqua, E. *J. Power Sources* **1999**, *77*, 136−142.

(3) Uchida, M.; Fukuoka, Y.; Sugawara, Y.; Eda, N.; Ohta, A. *J. Electrochem. Soc.* **1996**, *143*, 2245−2252.
(4) Thomas, S. C.; Ren, X.; Gottesfeld, S. *J. Electrochem. Soc.* **1999**, *146*, 4354−4359.
(5) Antolini, E.; Gonzalez, E. R. *Solid State Ionics* **2009**, *180*, 746−763.
(6) Antolini, E.; Gonzalez, E. R. *Appl. Catal., A* **2009**, *365*, 1−19.
(7) Reiser, C. A.; Bregoli, L.; Patterson, T. W.; Yi, J. S.; Yang, J. D.; Perry, M. L.; Jarvi, T. D. *Electrochem. Solid-State Lett.* **2005**, *8*, A273−A276.
(8) Taniguchi, A.; Akita, T.; Yasuda, K.; Miyazaki, M. *J. Power Sources* **2007**, *130*, 42−49.
(9) Ferreira, P. J.; la O, G . J.; Shao-Horn, Y.; Morgan, D.; Makharia, R.; Kocha, S.; Gasteiger, H. A. *J. Electrochem. Soc.* **2005**, *152*, A2256−A2271.
(10) Zhang, J.; Sasaki, K.; Sutter, E.; Adzic, R. R. *Science* **2007**, *315*, 220−222.
(11) Landsman, D. A.; Luczak, F. J. *Handbook of Fuel Cells Fundamentals, Technology, and Applications*; John Wiley & Sons: Chichester, U.K., 2003.
(12) Wu, G.; Chen, Y. S.; Xu, B. Q. *Electrochem. Commun.* **2005**, *7*, 1237−1243.
(13) Liang, Y. M.; Zhang, H. M.; Yi, B. L.; Zhang, Z. H.; Tan, Z. C. *Carbon* **2005**, *43*, 3144−3152.
(14) Hyeon, T.; Han, S.; Sung, Y. E.; Park, K. W.; Kim, Y. W. *Angew. Chem., Int. Ed.* **2003**, *42*, 4352−4356.
(15) Park, K. W.; Sung, Y. E.; Han, S.; Yun, Y.; Hyeon, T. *J. Phys. Chem. B* **2004**, *108*, 939−944.
(16) Yoshitake, T.; Shimakawa, Y.; Kuroshima, S.; Kimura, H.; Ichihashi, T.; Kubo, Y.; Kasuya, D.; Takahashi, K.; Kokai, F.; Yudasaka, M.; Iijima, S. *Phys. B* **2002**, *323*, 124−126.
(17) Bessel, C. A.; Laubernds, K.; Rodriguez, N. M.; Baker, R. T. K. *J. Phys. Chem. B* **2001**, *105*, 1115.
(18) Yuan, F. L.; Ryu, H. *J. Nanotechnology* **2004**, *15*, S596−S602.
(19) Shang, N.; Papakonstantinou, P.; Wang, P.; Silva, S. R. P. *J. Phys. Chem. C* **2010**, *114*, 15837−15841.
(20) Jang, S.-E.; Kim, H. *J. Am. Chem. Soc.* **2010**, *132*, 14700−14701.
(21) Santos, A. L.; Profeti, D.; Olivi, P. *Electrochim. Acta* **2005**, *50*, 2615−2621.
(22) Hagemeyer, A.; Hogan, Z.; Schlichter, M.; Smaka, B.; Streukens, G.; Turner, H.; Volpe, A.; Weinberg, J., H.; Yaccato, K. *Appl. Catal., A* **2007**, *217*, 139−148.
(23) Chhina, H.; Campbell, S.; Kesler, O. *J. Power Sources* **2006**, *161*, 893−900.
(24) Cui, X.; Shi, J.; Chen, H.; Zhang, L.; Guo, L.; Gao, J.; Li, J. *J. Phys. Chem. B* **2008**, *112*, 12024−12031.
(25) Rajeswari, J.; Viswanathan, B.; Varadarajan, T. K. *Mater. Chem. Phys.* **2007**, *106*, 168−174.
(26) Haas, O. E.; Briskeby, S. T.; Kongstein, O. E.; Tsypkin, M.; Tunold, R.; Borresen, B. T. *J. New Mater. Electrochem. Syst* **2008**, *11*, 9−14.
(27) Chen, G. Y.; Bare, S. R.; Mallouk, T. E. *J. Electrochem. Soc.* **2002**, *149*, A1092−A1099.
(28) Lasch, K.; Hayn, G.; Jorissen, L.; Garche, J.; Besenhardt, O. *J. Power Sources* **2002**, *105*, 305−310.
(29) Chen, Z.; Qiu, X.; Lu, B.; Zhang, S.; Zhu, W.; Chen, L. *Electrochem. Commun.* **2005**, *7*, 593−596.
(30) Zhu, X.; Zhang, H.; Y., L.; Zhang, Y.; Yia, B. *Electrochem. Solid-State Lett.* **2006**, *9*, A49−A52.
(31) Seger, B.; Kongkanand, A.; Vinodgopal, K.; Kamat, P. V. *J. Electroanal. Chem.* **2008**, *621*, 198−204.
(32) Ganesan, R.; Lee, J. S. *Angew. Chem., Int. Ed.* **2005**, *44*, 6557.
(33) Jeon, M. K.; Daimon, H.; Lee, K. R.; Nakahara, A.; Woo, S. I. *Electrochem. Commun.* **2007**, *9*, 2692−2695.
(34) Choi, D.; Kumta, P. N. *J. Am. Ceram. Soc.* **2007**, *90*, 3113−3120.
(35) Aromaa, J.; Forsén, O. *Electrochim. Acta* **2006**, *51*, 6104−6110.
(36) Nagarale, R. K.; Shin, W.; Singh, P. K. *Polym. Chem.* **2010**, *1*, 388−408.
(37) Antonucci, P. L.; Arico, A. S.; Creti, P.; Ramunni, E.; Antonucci, V. *Solid State Ionics* **1999**, *125*, 431−439.
(38) Dimitrova, P.; Friedrich, K. A.; Stimming, U.; Vogt, B. *Solid State Ionics* **2002**, *150*, 115.
(39) Anderson, Michele L.; Debra, R. M. S.; Rolison, R. *Nano Lett.* **2002**, *2*, 235−240.
(40) Sun, S. H.; Yang, D. Q.; Villers, D.; Zhang, G. X.; Sacher, E.; Dodelet, J. P. *Adv. Mater.* **2008**, *20*, 571−574.
(41) Schmidt, T. J.; Gasteiger, H. A.; Stab, G. D.; Urban, P. M.; Kolb, D. M.; Behm, R. J. *J. Electrochem. Soc.* **1998**, *145*, 2354−2358.
(42) Han, T.; Dale, N. V.; Adjemian, K.; Nallathambi, V.; Barton, S. C. *ECS Trans.* **2011**, *41*, 2289−2296.
(43) Guglielmi, M.; Colombo, P.; Rigato, V. *J. Electrochem. Soc.* **1992**, *139*, 1655−1661.
(44) Patterson, A. *Phys. Rev.* **1939**, *56*, 978−982.
(45) Kameyama, K.; Shohji, S.; Onoue, S.; Nishimura, K.; Yahikozawa, K.; Takasu, Y. *J. Electrochem. Soc.* **1993**, *140*, 1034−1037.
(46) Colomer, M. T.; Jurado, J. R. *Chem. Mater.* **2000**, *12*, 923−930.
(47) *CRC Materials Science and Engineering Handbook*, 3rd ed.; Shackelford, J. F., Alexander, W., Eds.; CRC Press: Boca Raton, FL, 2000.
(48) Kangasniemi, K. H.; Condit, D. A.; Jarvi, T. D. *J. Electrochem. Soc.* **2004**, *151*, E125−E132.
(49) Hu, C.-C.; Huang, Y.-H.; Chang, K.-H. *J. Power Sources* **2002**, *108*, 117−127.
(50) Sun, Y.; Zhuang, L.; Lu, J.; Hong, X.; Liu, P. *J. Am. Chem. Soc.* **2007**, *129*, 15465−15467.
(51) Roen, L. M.; Paik, C. H.; Jarvi, T. D. *Electrochem. Solid-State Lett.* **2004**, *7*, A19−A22.
(52) Williams, M. V.; Kunz, H. R.; Fenton, J. M. *J. Electrochem. Soc.* **2005**, *3*, A635−A644.
(53) Sambandam, S.; Ramani, V. *Electrochim. Acta* **2008**, *53*, 6328−6336.
(54) Sambandam, S.; Ramani, V. *Phys. Chem. Chem. Phys.* **2010**, *2*, 6140−6149.
(55) Rho, Y. W.; V, O. A.; Srinivasan, S. *J. Electrochem. Soc.* **1994**, *141*, 2084−2088.
(56) Gasteiger, H. A.; Kocha, S. S.; Sompalli, B.; Wagner, F. T. *Appl. Catal., B* **2005**, *56*, 9−35.